JOURNAL OF COMPUTATIONAL PHYSICS 106, 337–354 (1993)

Variational Algorithms and Pattern Formation in Dendritic Solidification

ROBERT ALMGREN

Department of Mathematics, The University of Chicago, Chicago, Illinois 60637

Received January 27, 1992; revised October 2, 1992

We present a completely new variational algorithm for computing dendritic solidification. This algorithm reproduces the Gibbs–Thomson relation as a balance between bulk and surface energy and is able to operate in the infinite-mobility limit with no unphysical time-step restriction. It may be used with arbitrary non-smooth surface energy functions and may include finite kinetic mobility. We perform computations with isotropic and anisotropic surface energy; from a small irregular initial seed we generate radial tip-splitting structures for isotropic energy and parabolic dendrites with side-branching for anisotropic energy. For anisotropic energy, the final structure is determined by the material and environmental properties; the initial shape is forgotten. For the parabolic dendrite tips, we obtain agreement with the Ivantsov solutions within a few percent and proper dimensional scaling of lengths and velocities with surface energy.

INTRODUCTION

The various phenomena associated with dendritic solidification are some of the most fascinating and important examples of spontaneous pattern formation in nature. One spectacular case is the growth of a snowflake in the atmosphere, following nucleation on a microscopic speck of dust. The final shape of the snowflake, often complex, symmetric, and beautiful, is determined by the atmospheric conditions and the physical properties of ice, air, water vapor, and the ice/vapor interface; the exact mechanisms are far from clear. Dendritic solidification is of immense practical importance: "*every day* nearly two million tons of steel are frozen: all of this steel has undergone a process of dendritic growth" [10]. Even a more modern application is zone refining of semi-conductor materials [32]; if the process is run too rapidly the interface becomes unstable and the product is of poor quality. From a scientific point of view we would like to understand how the shapes of snowflakes are created from vapor; from a practical point of view we need to understand how interfacial instability may be controlled or prevented.

In the 1930s and early 1940s, Nakaya [26] observed natural snowflakes, and classified their structures into several types: needle, plate, dendritic, etc. In an effort to understand how their shapes were determined, he built an experimental apparatus, in which he was ultimately able to reproduce all the naturally occurring shapes by varying two parameters: the air temperature and the supersaturation of water vapor. The celebrated "Nakaya diagram" identifies, for each point in the temperature–supersaturation plane, the unique type of snowflake growth which occurs under those conditions. In general, if these parameters changed with time, the instantaneous conditions determined the mode of growth at each moment, and he was able to identify a mapping between time histories of these two environmental parameters and final crystal shapes. Further experiments were performed by Kobayashi [20]. Since this mapping was consistently reproducible, we may believe that the experiments correctly identified the key factors which determine snowflake growth.

The computational project described in this paper is in the same spirit as Nakaya's experiments. In a computer model, we control not only the environmental parameters, but the physical laws themselves. If we are able to reproduce realistic shapes such as snowflakes or the dendritic microstructures of freezing metal, using a model which incorporates only a few physical effects, then we may believe that we have identified the key features of the problem.

We study a model system of equations which incorporates only anisotropic interfacial surface tension, as expressed in the Gibbs–Thomson condition, Eq. (1) below, and release and flow of latent heat of fusion as liquid freezes to solid (2). Interfacial instability arises due to the coupling between the shape of the interface and heat flow through the surrounding liquid, leading to dendritic shape generation. This system is believed to describe very well the freezing of a solid material from its liquid melt, as in the casting and zone refining examples mentioned above. Whether these effects are sufficient to explain the shapes of snowflakes is one of the questions this project is ultimately intended to answer.

In particular, one mechanism which we do not necessarily

0021-9991/93 $5.00

include in our model is finite kinetic mobility of the interface (the inverse mobility $\alpha > 0$ in (8) below). Our belief is that this effect, while certainly present physically to some extent, is not a necessary element of the pattern-generation mechanisms we are interested in. We would like first to understand the dynamics of solidification without this effect, the better to understand the consequences of including it. For the special case of snowflake growth, interfacial mobility may in fact be a controlling mechanism, as suggested by the numerical simulations of [39] which include only mobility and heat flow, but for solidification from a melt it is thought to be much less important.

The problem of diffusion-controlled solidification has attracted much theoretical interest. Linear stability analysis of advancing planar interfaces and growing spheres was studied in [24, 25], identifying the fundamental instability mechanism. More recently, attention has been focused on the role of small surface tension in stabilizing and in selecting shape and velocity of a dendritic tip [17]. For reviews of this work, see [18, 21].

In recent years, several numerical algorithms have been constructed for simulating this problem in its full geometrical complexity, most notably level-set formulation combined with boundary-integral methods [31], and phase-field models [9, 19, 38]. In general, these methods rely on introducing a finite kinetic coefficient $\alpha > 0$, in the sense that the computations necessarily become more and more expensive as $\alpha \to 0$. (Conformal mapping techniques [7] do not require finite kinetics, or even finite surface energy, but they apply only in two space dimensions and only in the "quasi-static" limit.) In this paper, we introduce an entirely new class of numerical methods which do not have this limitation; they work (in any dimension) for any value $\alpha \geqslant 0$ and the performance does not degrade in the infinite-mobility limit.

We take the point of view that the Gibbs–Thomson boundary condition (1) expresses an equilibrium between minimization of bulk and surface energy and design an algorithm which represents the time-dependent solution of the equations of motion as the limit of a sequence of solutions to a set of variational problems. This is fundamentally different from algorithms which extract an expression for the interface normal velocity in terms of local conditions such as temperature and curvature. Such formulations typically have stringent stability limits on the time step and require computation of interface curvature, a second derivative which can be very poorly behaved. Our algorithm has no unphysical time-step restrictions. The surface energy enters only as an integral; thus the formulation is well-defined, even for non-smooth and non-convex surface energy functions, and may be used to derive the correct form of the Gibbs–Thomson condition for those functions.

The research project whose computational results are described here has had as its original goal the numerical simulation of crystal growth. But understanding the problem sufficiently clearly to implement it on a computer required developing a new formulation, and this formulation was powerful enough to lead to new rigorous results. Convergence of the variational algorithm has been established [2, 22] (for the discrete-time, continuous-space version). Besides providing highly desirable support for the numerical work, this analysis establishes for the first time the existence of solutions to the model equations. This is a nice example of the interconnectedness of modern applied mathematics and the interplay between computation and theory.

The paper is organized into four sections: In Section 1 we review the equations which govern the physical problem, and present the Mullins–Sekerka stability analysis and a few exact solutions. In Section 2 we present a class of variational algorithms which are closely based on physical principles such as minimization of Gibbs free energy. In Section 3 we present a variational formulation derived from the formulations of Section 2, modified to be efficient enough for practical computation. We show how finite kinetic effects may be easily incorporated, and briefly discuss the numerical implementation. Section 4 contains results of two-dimensional computations. We first verify the correctness of the method using test problems with circular symmetry and zero surface energy, and we investigate robustness to perturbation of the interface position. We then present large-scale computations.

With the initial solid region as a small irregular seed, we generate large fingered structures. For isotropic surface energy, the structures have the tip-splitting form characteristic of radial growth. For anisotropic surface energy, parabolic dendrite tips emerge. We obtain quantitative agreement with Ivantsov solutions. To our knowledge, the only other general-purpose numerical methods to have reported such agreement are the related work described in [27, 28], in which the interface is modelled as a polygon with fixed normal directions given by the Wulff shape, and the very recent phase-field computations reported in [38].

In addition, we formulate a principle of remembering/forgetting the initial conditions, valid when the initial shape is not too different from a circle. For a small initial seed, the initial irregularities quickly relax to an "attracting" shape determined by the surface energy: round for isotropic, more polygonal for anisotropic. For a certain period, the seed grows, maintaining this shape; when it is large enough, instability sets in and fingers develop. For isotropic surface energy, although the seed is nearly round, the perturbations which start the instability are entirely provided by the initial conditions; thus basic features of the initial shape such as principal mode number and orientation are propagated into the large-scale structure.

For anisotropic surface energy, the attracting shape is a smoothed polygon, with mode number and orientation

determined by the surface energy function. This shape contains all the structure necessary to kick off the instability; the initial shape is completely forgotten.

We also verify proper scaling with the magnitude of surface energy, the only parameter in the problem. We identify one of our example computations as very inaccurate, although it has the correct value of the Peclet number and to the eye appears reasonable. The numerical errors are evidently such as to produce wrong values of the tip radius and velocity while generating the correct product.

1. THE PHYSICAL PROBLEM

1.1. Governing Equations

We are interested in describing the advance of a freezing front in a cooling liquid. Suppose $\Omega \subset R^d$ (dimension $d=2$ or 3) is a box full of a pure material which at each point at each time may be either liquid or solid, and let $\Sigma(t) \subset \Omega$ denote the solid region; the liquid region is the complement $\Omega \backslash \Sigma$. Let $T(x, t)$ denote the temperature field in Ω. Given an initial solid configuration Σ_0, an initial temperature field $T_0(x)$, and suitable boundary conditions for T on the box boundary $\partial\Omega$, the problem is to determine the subsequent evolution of $\Sigma(t)$ and of $T(x, t)$. For simplicity, we shall assume that the liquid/solid interface $\Gamma = \partial\Sigma$ does not come near the box edge $\partial\Omega$. We are especially interested in the "supercooled seed" configuration, in which Σ_0 is a small region near the center of Ω, and T decreases away from Σ into the liquid.

The geometry and the temperature field must be connected by suitable boundary conditions on Γ. In the simplest formulation which takes into account the surface energy of the liquid/solid interface, we impose the Gibbs–Thomson boundary condition ([13, 36]; see reviews [18, 21]), approximately valid when temperatures are not too far from the bulk melting temperature T_M and interface curvatures are not too large:

$$T = T_M\left(1 - \frac{\bar{\gamma}}{L}\mathscr{K}_\gamma\right) \quad \text{on} \quad \Gamma. \tag{1}$$

The surface energy per unit area $\gamma(\mathbf{n})$ is a function of the local surface normal direction $\mathbf{n}$; in (1), $\bar{\gamma}$ denotes the average of γ over $\mathbf{n}$, and $\mathscr{K}_\gamma$ denotes the "weighted mean curvature" [34] of Γ for the surface energy function $\gamma(\mathbf{n})$, which depends only on the anisotropic part $\gamma/\bar{\gamma}$. For smooth energy functions $\gamma(\mathbf{n})$, $\mathscr{K}_\gamma$ is a weighted sum of the principal curvatures of Γ; for isotropic surface energy $\gamma(\mathbf{n}) = \bar{\gamma}$, and $\mathscr{K}_\gamma$ is just the mean curvature (see (22) below). The constant L is the latent heat of fusion per unit volume. This condition expresses a local equilibrium between bulk and surface effects: for a bump of solid ($\mathscr{K} > 0$) to exist, the local temperature must be colder than T_M; otherwise the bump would immediately melt and pull back to reduce interface energy.

The evolution of the temperature field $T(x, t)$ is governed by two facts: first, that heat flows at a finite rate through the bulk material, and second, that as the interface advances and liquid turns to solid, latent heat of fusion L is released at the interface. The heat released in an interval of time in a neighborhood of Γ is L times the net volume of material which has changed from liquid to solid in that time interval. Thus $T(x, t)$ is the weak solution of the heat equation with singular source term

$$C\frac{\partial T}{\partial t} = \operatorname{div}(\kappa \nabla T) + LV(x, t)\,\delta_\Gamma \quad \text{in} \quad \Omega. \tag{2}$$

Here κ is the heat conductivity and C is the heat capacity per unit volume; for simplicity, we shall take both of these quantities to have the same value in the solid and the liquid phases. $V(x, t)$ is the local normal velocity of the interface Γ, positive if the freezing interface is advancing into the liquid, and δ_Γ is a Dirac mass concentrated on the hypersurface Γ.

In terms of the non-dimensional temperature

$$u = \frac{C}{L}(T - T_M),$$

and scaling time by a factor κ/C, (1) and (2) become

$$u = -\bar{\sigma}\mathscr{K}_\sigma \quad \text{on } \Gamma \tag{3}$$

$$\frac{\partial u}{\partial t} = \Delta u + V(x, t)\,\delta_\Gamma \quad \text{in } \Omega, \tag{4}$$

where

$$\bar{\sigma} = \frac{CT_M}{L^2}\bar{\gamma}$$

is a capillary length. Note that $\mathscr{K}_\sigma = \mathscr{K}_\gamma$ since $\sigma(\mathbf{n})$ and $\gamma(\mathbf{n})$ differ only by a scale factor.

It is sometimes convenient to split (4) into two heat equations

$$\frac{\partial u}{\partial t} = \Delta u \quad \text{in } \Sigma \text{ and } \Omega\backslash\Sigma \text{ separately}, \tag{4a}$$

together with a gradient jump condition at the interface,

$$V = -\left[\frac{\partial u}{\partial n}\right] = -\left.\frac{\partial u}{\partial n}\right|_L + \left.\frac{\partial u}{\partial n}\right|_S, \tag{4b}$$

where $\partial u/\partial n = \nabla u \cdot \mathbf{n}$ (u is necessarily continuous across Γ).

Thus the local velocity is equal to the rate of conduction of heat away from the interface.

Note also that we may easily reconstruct the temperature field given the interface history $\Gamma(t)$ (and hence the velocity $V(x, t)$ for x on $\Gamma(t)$) as

$$u(x, t) = \int_\Omega G_t(x-y)\, u_0(y)\, dy + \int_0^t \int_{\Gamma(s)} G_{t-s}(x-y)\, V(y, t)\, dS(y)\, ds. \quad (6)$$

Here $dS(y)$ denotes $(d-1)$-dimensional surface measure on Γ at y, and G_t is the d-dimensional heat kernel

$$G_t(x) = (4\pi t)^{-d/2} \exp(-|x|^2/4t). \quad (7)$$

This simple expression depends on the conductivities and capacities in solid and liquid being equal.

This model of solidification assumes that the interface is capable of advancing or retreating as fast as necessary to maintain the local equilibrium condition (3); its rate of advance is controlled only by the effectiveness of diffusion in dissipating its own latent heat. A finite kinetic rate of molecular attachment may be modeled by including a linear "velocity undercooling" term, replacing (3) by

$$u = -\bar{\sigma}\mathscr{K}_\sigma - \alpha(\mathbf{n})\, V, \quad (8)$$

where $\alpha(\mathbf{n}) > 0$ is an additional anisotropic material parameter, an inverse mobility. This term is very strongly regularizing [33]; but while we will see below that inclusion of finite surface tension ($\sigma > 0$) is necessary to obtain a linearly well-posed problem, inclusion of finite kinetics ($\alpha > 0$) is not necessary. In fact, the problem described by (8) is of an essentially different character than that described by (3), much more similar to the geometric models discussed in [35] in which the velocity of the interface is explicitly determined by the local environment. Our primary goal in the work presented in this paper has been to develop a method which directly attacks the difficulties presented by (3), that is, a method which works uniformly well in the limit $\alpha \to 0$. Hence we shall concentrate our attention on the equilibrium formulation (3), and in Section 3 we discuss how to extend the variational formulation to model (8).

Remark. For simplicity, we have assumed the heat conductivities and capacities to be the same in the solid and the liquid. This is not entirely realistic; for example, near 0°C the heat conductivity of ice is roughly four times that of liquid water, and the heat capacity is roughly half [15]. The algorithm presented in this paper may easily be generalized to handle two different conductivities, as long as neither one is very small; we have not written the details because in most solidification problems of realistic interest nearly all the heat flows through one phase (usually liquid). Modeling different heat capacities is substantially more complicated; among other difficulties, the latent heat must depend on temperature. The more complete situation is analysed in [2].

Remark. The same system, (3) and (4), results if one considers the isothermal solidification of a liquid containing a dissolved impurity [21], for example as in Ostwald ripening. Then u represents the chemical potential, a separate linear function of solute concentration in solid and in liquid; again u must be continuous across Γ. The latent heat L is replaced by the "miscibility gap."

Remark. A related two-dimensional system arises in the Hele–Shaw flow [29], a viscous fluid pushed by air between two plates, where u represents pressure in the liquid. In that problem, surface tension is usually isotropic, the field quantity exists u only on one side of the interface, and, most importantly, u does not diffuse but satisfies Laplace's equation with the boundary condition (3), so that knowledge of the interface position at any time determines the field in all space at that time: the field has no history. This "quasi-static" model is a natural limiting case of dendritic solidification, for small undercooling and slow growth. Our algorithm is not uniformly efficient in that limit.

1.2. Example Solutions

Very few analytical solutions are available for the problem (3), (4), except in very special cases. This is precisely the motivation for developing numerical simulation methods; they are the most effective way to study large-amplitude solutions of the full system. We shall briefly describe three special solutions: the Mullins–Sekerka linear instability of a flat interface, Frank's similarity solutions for growing spheres, and Ivantsov needle crystals. For simplicity, in these examples we take isotropic surface energy: $\sigma(\mathbf{n}) = \sigma$ constant. These solutions will later be useful as points of reference for our numerics.

Mullins–Sekerka Analysis

One solution of (3), (4) is the steadily advancing planar interface (Ω = all of R^2 or R^3)

$$\Sigma(t) = \{x < Vt\}$$
$$u(x, t) = u_0(x, t) = \begin{cases} 0, & x < Vt \\ -1 + e^{-V(x-Vt)}, & x > Vt \end{cases} \quad (9)$$

for any V; the undercooling u_∞ has the unique value -1. The Mullins–Sekerka analysis [25] essentially consists in

the observation that, to first order in ε, the perturbed interface

$$x = Vt + \varepsilon e^{\lambda t} \sin ky \qquad (k > 0)$$

and the perturbed temperature field

$$u(x, t) = u_0(x, t) + \varepsilon e^{\lambda t} \sin ky \times \begin{cases} Ae^{-\mu_+(x - Vt)} + Be^{-V(x - Vt)}, & x > Vt \\ Ce^{\mu_-(x - Vt)}, & x < Vt \end{cases}$$

solve (3), (4) if

$$\lambda(k, V) = 2k(\sigma k(k^2\sigma - V) - (k^2\sigma - \tfrac{1}{2}V)\sqrt{1 + \sigma(k^2\sigma - V)}). \quad (10)$$

The other coefficients $\mu_\pm$, A, B, and C are also determined as functions of k and V. If $V > 0$, then for $0 < k < k_{\text{crit}}(V)$ the interface is unstable to disturbances of wavenumber k, that is, $\lambda(k, V) > 0$, where

$$k_{\text{crit}}^2 = \frac{V}{8\sigma}(4 - \sigma V - \sqrt{\sigma V(8 + \sigma V)}) \approx \frac{1}{2}\frac{V}{\sigma}, \qquad \sigma V \ll 1. \quad (11)$$

As velocity increases or surface tension decreases, the band of unstable wavenumbers increases.

In a negative temperature gradient, long-wavelength disturbances grow while short-wavelength ones are killed by surface tension. Similar results hold for growing spheres and circles [24], and it is this instability which grows into dendritic arms. This is the essential feature of spontaneous pattern formation: the system generates structure on macroscopic length scales but is well-posed on small length scales. By contrast, the classical Stefan problem with $\sigma = 0$ has $\lambda = kV$ and is therefore either linearly ill-posed if $V > 0$ (arbitrarily small-amplitude high-frequency perturbations of the initial data grow arbitrarily rapidly) or completely stable if $V < 0$.

The mechanism of instability is quite simple and general. We have noted that the local rate of advance of the interface is controlled by how effectively it can dissipate its own heat. In a surrounding cold bath, a convex bump has locally enhanced heat dissipation and grows more rapidly than the neighboring hollows. Surface tension acts in the opposite direction, more effectively for short wavelengths. Since the instability mechanism is local to the interface, the surrounding temperature field need not have the exact form (9); any field with instantaneous normal gradient V may be expected to give the same dispersion relation (10) and stability limit (11).

Frank Spheres

Despite the above demonstration that an advancing interface is more and more unstable as $\sigma \to 0$, it is possible to construct formal solutions with $\sigma = 0$ and completely smooth initial data. One class of such solutions is the growing spheres developed by Frank [12] in one, two, and three space dimensions.

For dimension $d = 1$, 2, or 3, the solid region is the interior of the slab, cylinder, or sphere of radius,

$$R(t) = St^{1/2}, \quad (12)$$

parametrized by S, and the temperature field is

$$u(r, t) = u(s) = \begin{cases} 0, & s < S \\ u_\infty \cdot \left(1 - \dfrac{F_d(s)}{F_d(S)}\right), & s > S \quad (s = r/t^{1/2}). \end{cases} \quad (13)$$

The functions $F_d(s)$, similarity solutions of the heat equation, are

$$F_1(s) = \operatorname{erfc}\left(\frac{1}{2}s\right), \quad F_2(s) = E_1\left(\frac{1}{4}s^2\right), \quad F_3(s) = \frac{1}{s}\exp\left(-\frac{1}{4}s^2\right) - \frac{1}{2}\sqrt{\pi}\operatorname{erfc}\left(\frac{1}{2}s\right), \quad (14)$$

in which the special functions are

$$\operatorname{erfc}(z) = \frac{2}{\sqrt{\pi}}\int_z^\infty e^{-t^2}\,dt, \qquad E_1(z) = \int_z^\infty \frac{e^{-t}}{t}\,dt.$$

The undercooling $u_\infty < 0$ and the velocity parameter S are related by the jump condition (4b), which gives finally

$$u_\infty = \tfrac{1}{2}SF_d(S)/F_d'(S). \quad (15)$$

For a given undercooling, this may be solved numerically for S. As $u_\infty \searrow -1$, the speed $S \nearrow \infty$. For $d = 1$ this is not inconsistent with the finite-velocity planar solutions (9): in the latter, the decay of $u(x)$ as $x \to \infty$ is much slower than the Green's function (7), hence the initial heat distribution $u_0(x)$ must extend to ∞. In (13), the initial conditions are constant temperature $u = u_\infty$.

Although these solutions are obtained for $\sigma = 0$, the evidence is that the primary role of small nonzero surface energy is to stabilize the interface, rather than to modify the overall behavior. A rough estimate of the maximum stable

size of a growing circle in two dimensions may be obtained from the Mullins–Sekerka analysis. From (12), the local normal interface velocity is $V(R) = \frac{1}{2}S^2/R$. The mth mode of the circle has wavenumber $k = m/R$, and if (11) applies, it is stable for

$$R < R_{\text{crit}} = \frac{4m^2\sigma}{S^2}. \tag{16}$$

Our computations in Section 4 show that this formula is very approximate. Determining stability of a sphere in three dimensions requires study of the spherical harmonics as in [24].

Ivantsov Parabolas

The other class of known exact solutions is the Ivantsov parabolas [16], for vanishing surface tension $\sigma = 0$ (see reviews [21, 18]). In these solutions, the solid is the interior (to the left) of the parabola

$$x = -\frac{r^2}{2\rho} + Vt,$$

where $r^2 = y^2$ (2D) or $y^2 + z^2$ (3D), and ρ is the radius of curvature at the tip. With $\sigma = 0$, the temperature $u = 0$ inside the needle, and outside, $u \to u_\infty$ as $|(x, r)| \to 0$. The undercooling u_∞ is related to the Peclet number

$$p = \tfrac{1}{2}\rho V \tag{17}$$

by

$$u_\infty = \begin{cases} -\sqrt{\pi p}\, e^p \operatorname{erfc}(\sqrt{p}) & \text{(2D)} \\ -pe^p E_1(p) & \text{(3D).} \end{cases} \tag{18}$$

In the planar limit $p \to \infty$, the undercooling $u_\infty \to -1$ in accordance with the planar solution (9). As discussed above, with $\sigma = 0$ these solutions are completely unstable to small-amplitude high-frequency perturbations.

Unlike the Frank spheres, the Ivantsov needles are observed in experiments. Small surface tension $\sigma \neq 0$ introduces only a small modification of the tip shape, and since the tip is continually advancing, the instability is continually swept back from it [8].

For a specified undercooling u_∞, the above solution determines only the product ρV, not the tip width or velocity separately. A major accomplishment of the last few years has been the clarification of the role played by small $\sigma > 0$ in selecting one solution out of this family, and the role of anisotropy [17].

2. VARIATIONAL ALGORITHMS

The Gibbs–Thomson relation (3) is a local equilibrium condition: in some appropriate sense the interface continually adjusts itself to balance bulk energy and surface energy. It is natural to wonder whether this may be interpreted as the continual minimization of some combined energy. In this section we construct a class of such variational formulations of the equations of motion (3) and (4).

2.1. The Variational Approach

The variational method is a discrete-time formulation. Thus, we choose a time step Δt and generate a sequence of solid configurations $\Sigma_0, \Sigma_1, \ldots$, and temperature fields $u_0(x)$, $u_1(x), \ldots$, representing an approximation to the solution at times $0, \Delta t, 2\Delta t, \ldots$. Initial data Σ_0, $u_0(x)$ are specified, which may or may not satisfy the Gibbs–Thomson condition (3). We must determine Σ_{n+1}, u_{n+1} from Σ_n, u_n.

At the nth step, we define an *energy functional* $\mathscr{E}^n(\Sigma)$ which associates an energy value to every possible configuration Σ which the interface might assume at step $n+1$; this energy function depends on Σ_n and u_n. Then the next configuration Σ_{n+1} is determined by the simple prescription

$$\Sigma_{n+1} \text{ minimizes } \mathscr{E}^n(\Sigma), \tag{19}$$

where the minimum should be taken over all possible configurations, not just those which are "close" to Σ_n. Of course, $\mathscr{E}^n(\Sigma)$ should be such that, most of the time, Σ_{n+1} is reasonably well behaved and is in fact close to Σ_n, and so that in the limit $\Delta t \to 0$ the sequence $\{\Sigma_n\}$ converges to a smooth evolution $\Sigma(t)$ with finite normal velocity V. Once Σ_{n+1} has been determined, the new temperature u_{n+1} is determined in a straightforward analog of (6).

In designing a variational algorithm, the object is to choose $\mathscr{E}^n$ so that the stationarity conditions which any smooth local minimum must satisfy are exactly the Gibbs–Thomson condition. In this paper, we shall not address questions of existence and regularity of the minimizing Σ_{n+1}. We will generally choose functions for which existence and regularity are plausible and refer to rigorous results where they are known for appropriate choices of $\mathscr{E}^n$.

One component of $\mathscr{E}^n(\Sigma)$ must certainly be the surface energy of Σ. Recalling that $\sigma(\mathbf{n})$ is the surface energy per unit area for surface with normal direction $\mathbf{n}$, we define

$$\mathscr{E}_S(\Sigma) = \int_\Gamma \sigma(\mathbf{n}(x))\, dS(x) \qquad (\Gamma = \partial\Sigma), \tag{20}$$

where $dS(x)$ denotes arc length in two dimensions, surface area in three. The surface energy $\mathscr{E}_S$ does not depend on the previous configuration Σ_n, u_n.

If we describe a variation $\delta\Sigma$ of the geometry by a smooth

function $\delta\rho(x)$ denoting normal displacement, then the first variation of $\mathscr{E}_S(\Sigma)$ may be written [23, 34]

$$\delta\mathscr{E}_S = \bar{\sigma}\int_\Gamma \mathscr{K}_\sigma(x)\,\delta\rho(x)\,dS(x). \tag{21}$$

As noted below (1), $\bar{\sigma}$ is the mean value of $\sigma(\mathbf{n})$, and $\mathscr{K}_\sigma$ is the weighted mean curvature of Γ, for surface energy function $\sigma(\mathbf{n})$. In two dimensions, for a smooth surface energy function $\sigma(\theta)$, we may write

$$\tilde{\sigma}\mathscr{K}_\sigma = \tilde{\sigma}(\theta)\mathscr{K},$$

where $\tilde{\sigma}$ is a surface tension

$$\tilde{\sigma}(\theta) = \sigma''(\theta) + \sigma(\theta) \tag{22}$$

and $\mathscr{K}$ is simply the curvature of Γ.

The integral (20) is defined for very non-smooth surfaces and energy, and Taylor [34] has used appropriate analogs of (21) to define weighted mean curvature and motion by weighted mean curvature for general crystalline energy integrands $\sigma(\mathbf{n})$ and polyhedral surfaces Γ. That formulation may be carried over into the present problem. Including surface energy only as an integral, from which the Gibbs–Thomson relation emerges as a variational condition, makes the variational algorithms described here extremely flexible and conceptually powerful.

The other element which must enter the energy functional $\mathscr{E}^n(\Sigma)$ is a bulk energy term $\mathscr{E}^n_V(\Sigma)$. Below we present several alternative forms, but all involve a temperature field: an approximation to the field which would exist at the end of this time step if the interface moved from Γ^n to the candidate position Γ.

The interface advances from Γ^n to Γ if the material in between has frozen; similarly, it retreats if material melts. Change of phase means local release or absorption of latent heat. If heat flow could be ignored, the resulting temperature field would be

$$u_n + \chi_\Sigma - \chi_{\Sigma_n},$$

where χ_Σ, χ_{Σ_n} are the characteristic functions of Σ, Σ_n. (The heat content of each point, $u(x) - \chi(x)$, is constant for phase change without heat flow.) However, heat flow is an essential part of the problem.

The temperature field which we actually do associate with any test position Σ during the step from n to $n+1$ is the above temperature field subjected to a suitable amount of heat flow,

$$u^n_\Sigma = G_{\Delta t} * u_n + G_{\Delta t/2} * (\chi_\Sigma - \chi_{\Sigma_n}), \tag{23}$$

where G is the heat kernel from (7). The heat present from the previous step is "flowed" for a full step Δt. The latent heat released by the motion is flowed for half a time step $\Delta t/2$, as though it were all released at $t = (n+\frac{1}{2})\,\Delta t$. We ignore interaction with the box boundary.

This definition incorporates two essential elements: the interface may never move without releasing or absorbing latent heat; and the resulting discontinuous temperature field must always be "smeared" for a time proportional to Δt before it is used. In a certain sense, we are not allowed to look at the system with a time precision finer than Δt. The exact multipliers of Δt in (23) are not critical; in fact, convolution with the fixed kernel $G_{\Delta t}$ may be replaced by transport of heat so as to minimize the Dirichlet integral, subject to a constraint on the maximum transport distance [2].

Let us note the first variation of $\delta u^n_\Sigma(x)$ with respect to small changes $\delta\Sigma$, described again by a small normal displacement $\delta\rho(x)$. Since heat is released or absorbed only on the interface,

$$\delta u^n_\Sigma(x) = \int_\Gamma G_{\Delta t/2}(x-y)\,\delta\rho(y)\,dS(y)$$

for $x \in \Omega$.

We may now complete the definition of the energy $\mathscr{E}^n(\Sigma)$. We choose a function $F(u, \phi)$, where ϕ takes the values 0 and 1, and define

$$\mathscr{E}^n_V(\Sigma) = \int_\Omega F(u^n_\Sigma, \chi_\Sigma)\,dx$$

and

$$\mathscr{E}^n(\Sigma) = \mathscr{E}^n_V(\Sigma) + \mathscr{E}_S(\Sigma).$$

Below we present two different choices of $F(u, \phi)$, both of which give rise to the Gibbs–Thomson relation.

Choice of F tells us how to obtain the next interface position Σ_{n+1}. We complete the algorithm by specifying the temperature field u_{n+1} for the next step as

$$u_{n+1} = u^n_{\Sigma_{n+1}}. \tag{24}$$

If the $\{\Sigma_n\}$ converge to some $\Sigma(t)$ as $\Delta t \to 0$, then the $\{u_n(x)\}$ converge to $u(x, t)$ which satisfies (4): clearly the heat equation is correctly approximated away from $\Gamma(t)$, thus (4a); and heat is conserved in the neighborhood of $\Gamma(t)$, thus (4b). By virtue of (24), whatever stationarity conditions are satisfied by the minimizing Σ_n are satisfied by $\Sigma(t)$ and $u(t)$ at each time $t = n\,\Delta t$. This heuristic reasoning may be made rigorous for the second example below.

2.2. Two Example Functionals

"Free Energy" Function

If temperature and pressure are held constant, a bulk material changes phase so as to minimize its Gibbs free energy. This principle may be used to obtain the Gibbs–Thomson relation as a necessary condition for a stationary equilibrium configuration [18, 13]. However, time-dependent solidification is a non-equilibrium phenomenon and, as emphasized above, phase changes are necessarily accompanied by temperature changes (see the discussion of nucleation below). For these reasons, the relevance of free energy is not entirely clear. We take the Gibbs–Thomson relation as an empirically verified fact and present the following in the spirit of a mathematical construction.

We take the energy function

$$F(u, \phi) = \begin{cases} \frac{1}{2}u, & \phi = 1, \\ -\frac{1}{2}u, & \phi = 0. \end{cases}$$

Just as for the physical free energy, F is minimized at a fixed $u > 0$ if $\phi = 0$, corresponding to liquid; for $u < 0$, solid with $\phi = 1$ is preferred. This function linearly penalizes supercooled liquid or superheated solid. Thus, minimization of $\mathscr{E}^n(\Sigma)$ may be thought of as the instruction that the material should minimize its total (bulk + surface) free energy at each time step, subject to the constraints that interface motion releases heat, and that in one step, heat may diffuse no farther than appropriate for the step length Δt. This is essentially the same energy function considered in [37] for minimization in a predetermined temperature field.

The first variation of $\mathscr{E}^n_V$ is

$$\begin{aligned} \delta\mathscr{E}^n_V &= \delta\left(\int_\Sigma \tfrac{1}{2}u^n_\Sigma\,dx - \int_{\Omega\setminus\Sigma} \tfrac{1}{2}u^n_\Sigma\,dx\right) \\ &= \int_\Sigma \tfrac{1}{2}\delta u^n_\Sigma(x)\,dx - \int_{\Omega\setminus\Sigma} \tfrac{1}{2}\delta u^n_\Sigma(x)\,dx \\ &\quad + \int_{\partial\Sigma} u^n_\Sigma\,\delta\rho(x)\,dS(x). \end{aligned}$$

The first two terms cancel to leading order in Δt (the interface appears planar on length scales $\mathcal{O}(\Delta t^{1/2})$, so heat released on the interface flows half into the solid, half into the liquid), and the total energy change is

$$\delta\mathscr{E}^n = \delta\mathscr{E}^n_V + \delta\mathscr{E}_S = \int_\Gamma (u^n_\Sigma + \bar\sigma\mathscr{K}_\sigma)\,\delta\rho(x)\,dS(x).$$

Thus, Σ can minimize $\mathscr{E}^n$ only if

$$u^n_\Sigma + \bar\sigma\mathscr{K}_\sigma = 0 \qquad \text{on } \Gamma,$$

the Gibbs–Thomson condition.

Note that although $\mathscr{E}^n(\Sigma)$ is minimized at each step, the sequence of minimum values $\mathscr{E}^n(\Sigma_n)$ may increase. $\mathscr{E}^n(\Sigma_n)$ differs from $\mathscr{E}^{n-1}(\Sigma_n)$ by convolution of u^n with $G_{\Delta t}$, and it may happen that $\mathscr{E}^n(\Sigma_n) > \mathscr{E}^{n-1}(\Sigma_n)$. Thus, although the minimization guarantees that $\mathscr{E}^n(\Sigma_{n+1}) \leqslant \mathscr{E}^n(\Sigma_n)$ and $\mathscr{E}^{n-1}(\Sigma_n) \leqslant \mathscr{E}^{n-1}(\Sigma_{n-1})$, we may not conclude that $\mathscr{E}^n(\Sigma_n) \leqslant \mathscr{E}^{n-1}(\Sigma_{n-1})$ or that $\mathscr{E}^n(\Sigma_{n+1}) \leqslant \mathscr{E}^{n-1}(\Sigma_n)$. Of course, physically we expect the system to proceed in the direction of decreasing free energy.

Lyapunov Function

Our second example is

$$F(u, \phi) = \tfrac{1}{2}u^2,$$

independent of ϕ. The first variation of $\mathscr{E}^n_V$ is

$$\delta\mathscr{E}^n_V = \int_\Omega u^n_\Sigma(x)\,\delta u^n_\Sigma(x)\,dx = \int_\Gamma \bar u^n_\Sigma(y)\,\delta\rho(y)\,dS(y),$$

where

$$\bar u^n_\Sigma(x) = \int_\Omega G_{\Delta t/2}(x - y)\,u^n_\Sigma(y)\,dy$$

is a locally averaged temperature which approaches $u^n_\Sigma(x)$ as $\Delta t \to 0$. Again the stationarity condition is

$$\bar u^n_\Sigma + \bar\sigma\mathscr{K}_\sigma = 0 \qquad \text{on } \Gamma$$

and if a limit exists as $\Delta t \to 0$, the limit function must satisfy the Gibbs–Thomson relation.

In this case, $\mathscr{E}^n_V$ decreases under heat flow, so $\mathscr{E}^n(\Sigma_n) \leqslant \mathscr{E}^{n-1}(\Sigma_n)$ and $\mathscr{E}^n(\Sigma_n)$ is nonincreasing, making rigorous estimates possible. Existence of the minimum at each step, and convergence almost everywhere as $\Delta t \to 0$, have been demonstrated in [22]. Existence and convergence have been demonstrated in [2] for the highly nontrivial extension to nonequal heat diffusivities and especially heat capacities.

Numerical calculations using a direct implementation of this method have been presented in [3], obtaining agreement with the Mullins–Sekerka stability theory for planar interfaces. That implementation is far too inefficient to compute complicated shapes; for realistic simulation the approximate-temperature formulation of Section 3 must be used.

2.3. Nucleation, Jumps, and Nonuniqueness

We conclude this section by briefly describing three additional interesting aspects of the variational method.

Nucleation

For any temperature $u_0(x)$, the configurations $\Sigma = \varnothing$ (all liquid) and $\Sigma = \Omega$ (all solid) are local minima, but not necessarily global minima. Suppose for simplicity that the initial temperature $u_0 < 0$ is constant and that $\Sigma_0 = \varnothing$, and let us consider nucleation of round solid seeds; that is, let us compute the energy of configurations $\Sigma(R) = \{|x| < R\}$.

The temperature $u_\Sigma = u_0 + G_{\Delta t/2} * \chi_\Sigma$. If $R \ll \Delta t^{1/2}$, then the seed is like a point source of heat, with total heat release equal to its volume $\omega_d R^d$, and

$$u_\Sigma(x) \approx u_0 + \omega_d R^d G_{\Delta t/2}(x) \qquad (R \ll \Delta t^{1/2}),$$

where ω_d is the volume of the d-dimensional unit sphere. If $R \gg \Delta t^{1/2}$, then heat flow may essentially be neglected and, for purposes of integration,

$$u_\Sigma(x) \approx \begin{cases} u_0 + 1, & |x| < R \\ u_0, & |x| > R \end{cases} \qquad (R \gg \Delta t^{1/2}).$$

The surface energy of the seed is

$$\mathscr{E}_S(\Sigma) = \sigma d \omega_d R^{d-1}.$$

In the free-energy formulation,

$$\mathscr{E}_V(\Sigma) = \tfrac{1}{2}\int_\Sigma u_\Sigma - \tfrac{1}{2}\int_{\Omega\setminus\Sigma} u_\Sigma = -\tfrac{1}{2}\int_\Omega u_\Sigma + \int_\Sigma u_\Sigma.$$

If $R \ll \Delta t^{1/2}$, this becomes

$$\mathscr{E}_V(\Sigma) \approx -\tfrac{1}{2}\int_\Omega u_0 - \tfrac{1}{2}\omega_d R^d + (u_0 + \omega_d R^d G_{\Delta t/2}(0))\,\omega_d R^d,$$

since $\int G_t = 1$, and so

$$\mathscr{E}_V(\Sigma) - \mathscr{E}_V(\Sigma_0) \approx (d\sigma + (u_0 - \tfrac{1}{2})R)\,\omega_d R^{d-1} \qquad (R \ll \Delta t^{1/2}).$$

Note that, contrary to our intuition for systems maintained at a fixed temperature, the free energy reduction resulting from reducing the undercooling in the surrounding liquid is actually more important than the free energy reduction from the phase change within the seed (if $|u_0| < \frac{1}{2}$). This is a consequence of the finite time step Δt: heat does not reach the boundaries and vanish into a reservoir.

If $R \gg \Delta t^{1/2}$, then

$$\int_\Omega u_\Sigma \approx \int_\Omega u_0 + \omega_d R^d, \qquad \int_\Sigma u_\Sigma \approx (u_0 + 1)\,\omega_d R^d,$$

and hence

$$\mathscr{E}_V(\Sigma) - \mathscr{E}_V(\Sigma_0) \approx (d\sigma + (u_0 + \tfrac{1}{2})R)\,\omega_d R^{d-1} \qquad (R \gg \Delta t^{1/2}).$$

We may then observe that

1. If $u_0 < -\frac{1}{2}$, then $\mathscr{E}(\Sigma) < \mathscr{E}(\Sigma_0)$ for large R and nucleation occurs. In fact, $\mathscr{E}(\Sigma)$ decreases without bound as $R \to \infty$ and the global minimum is to freeze the whole box ($\Sigma = \Omega$).

2. If $u_0 < 0$ is close enough to zero and σ is large enough, then it is plausible that $\mathscr{E}(R) > \mathscr{E}(\Sigma^0)$ for all $R > 0$, and nucleation does not occur. This is the reason we may look for minimizing configurations only close to Σ_0: we do not have to consider adding new pieces of solid in every region of undercooled liquid.

In the case of quadratic energy, as discussed in [22], the calculations and conclusions are similar. We find

$$\mathscr{E}(\Sigma) - \mathscr{E}(\Sigma_0) \approx (d\sigma + 2u_0 R)\,\omega_d R^{d-1} \qquad (R \ll \Delta t^{1/2})$$

and

$$\mathscr{E}(\Sigma) - \mathscr{E}(\Sigma_0) \approx (d\sigma + (2u_0 + 1)R)\,\omega_d R^{d-1} \qquad (R \gg \Delta t^{1/2});$$

The same conclusions apply.

"Jumps"

Luckhaus [22] has shown that for the Lyapunov formulation, the globally minimizing Σ_{n+1} is not always arbitrarily close to Σ_n as $\Delta t \to 0$. In the neighborhood of changes of topology, for example as two pieces of solid or two parts of the solid approach each other to merge, there is always a finite distance h such that when they are within distance h it becomes energetically favorable to "jump the gap" and form a bridge; h does not go to zero as $\Delta t \to 0$. The formulation in [22] includes an additional parameter Λ, which does not affect smooth motion, but increasing Λ reduces the jump h.

Nonuniqueness

The Mullins–Sekerka instability has a discrete-time analog. If one considers a planar interface at $x = 0$, in a temperature field $u_0(x)$ with $u_0(0) = 0$, then one may study the energy $\mathscr{E}(\Sigma)$ for interface configurations of the form $x = a\sin(ky - \phi)$, as a function $E(a)$ for fixed k; by symmetry, E is independent of ϕ. One determines that (1) $E'(0) = 0$, as required by the symmetry $\phi \to \phi + \pi$, and (2) $E''(0) < 0$ if $u_0'(x)$ is sufficiently negative in a neighborhood of the origin. Thus the minimizing configuration must have $a \neq 0$, and since the phase ϕ is arbitrary this is a spontaneous

symmetry breaking for finite Δt. As $\Delta t \to 0$, the amplitude a of the minimizing configuration approaches zero, so that the continuous evolution $\Sigma(t)$ is the planar solution corresponding to the planar initial data.

3. AN EFFICIENT VARIATIONAL ALGORITHM

The variational algorithms presented in the last section, although elegant and appealing, are essentially completely impractical for actual computation, because of the need to model the heat diffusion for each test position. In this section, we present an efficient, practical variational algorithm, which relies on an estimation of the heat flow, precomputed in each step before the minimization of interface energy is begun.

We first present the two key steps in the approximate formulation, in the same discrete-time, continuous-space formulation which was used in Section 2, then show how the method may be extended to finite kinetic mobility, and briefly discuss the actual discrete representation in the computer.

3.1. Temperature Approximation

The first step in constructing the practical variational algorithm is the precomputation of an approximate temperature field $H^n(x)$. In the formulation of Section 2, the temperature field $u^n_\Sigma(x)$ associated with every candidate position Σ is a function of all $x \in \Omega$. But in fact, the only relevant values of u^n_Σ are those on the potential new interface Γ. With this motivation, we approximately define the single function $H^n(x)$ as

$$H^n(x) \approx \begin{cases} u^n_\Sigma(x), \text{ where } \Sigma \text{ is such that the new} \\ \text{interface } \Gamma = \partial\Sigma \text{ passes through } x, \\ \text{and } \Gamma \text{ is locally parallel to } \Gamma_n. \end{cases}$$

This is well defined and may be further approximated, under the assumption that the heat diffusion radius $\Delta t^{1/2}$ is everywhere intermediate between the two lengths

$V\,\Delta t$, the normal motion of the interface in time Δt,

$\mathscr{K}^{-1}$, the local radius of curvature,

which is true asymptotically as $\Delta t \to 0$ for a smooth interface moving at finite speed V. Then heat flow is locally one-dimensional and we write

$$H^n(x) = G_{\Delta t} * u_n + s\rho_n(x), \tag{25}$$

where the "normal slope" s is the value at the origin of the one-dimensional Green's function

$$s = G^1_{\Delta t/2}(0) = (2\pi\,\Delta t)^{-1/2}$$

and $\rho_n(x)$ is the signed distance from x to the starting position Γ_n:

$$\rho_n(x) = \begin{cases} \operatorname{dist}(x, \Gamma_n), & x \in \Omega \backslash \Sigma_n \\ -\operatorname{dist}(x, \Gamma_n), & x \in \Sigma_n, \end{cases}$$

where $\operatorname{dist}(x, \Gamma_n)$ denotes the usual distance from a point to a set

$$\operatorname{dist}(x, \Gamma) = \inf_{y \in \Gamma} |x - y|.$$

This function is well defined for arbitrarily complicated Γ_n, and if Γ_n is smoothly curved, $\rho_n(x)$ is smooth in a neighborhood of Γ_n (to a distance equal to the shortest radius of curvature of Γ_n), with $|\nabla\rho_n| = 1$.

Once the function H^n has been precomputed, the new interface Σ_{n+1} is determined by the minimization prescription (19) with

$$\mathscr{E}^n(\Sigma) = \int_\Sigma H^n(x)\,dx + \mathscr{E}_S(\Sigma).$$

This problem is known as the "prescribed mean curvature problem" because the stationarity condition is

$$H^n + \bar{\sigma}\mathscr{K}_\sigma = 0. \tag{26}$$

It has been extensively studied [14, 37], and effective numerical algorithms have been developed [5, 6]. Existence of the minimum at each step is essentially guaranteed for Δt small enough, since $|H^n|$ increases rapidly, with gradient $\mathcal{O}(\Delta t^{-1/2})$, away from Γ_n. Thus nucleation is not a concern in this model.

The approximation (25) is used only to determine the new interface position. Once we have determined Σ_{n+1}, we evaluate the new temperature u_{n+1} by (23) and (24). Under the assumptions that the interface is smooth and smoothly moving,

$$H^n(x) \approx u^n_\Sigma(x) = u_{n+1}(x), \qquad x \quad \text{on } \Gamma_{n+1},$$

and, by virtue of (26), the Gibbs–Thomson condition is approximately satisfied at the end of the step.

Remark. The details of the above formulation are quite robust. In general, we may introduce four parameters $\alpha_1, \alpha_2, \alpha_3, \beta$, and define an algorithm by

$$H^n = G_{\alpha_1 \Delta t} * u_n + s\rho_n, \qquad s = (4\pi\,\alpha_2\,\Delta t)^{-\beta}$$

$$\Sigma_{n+1} \text{ minimizes } \mathscr{E}^n(\Sigma)$$

$$u_{n+1} = G_{\Delta t} * u_n + G_{\alpha_3 \Delta t} * (\chi_{\Sigma_{n+1}} - \chi_{\Sigma_n}).$$

Here α_1 represents a "pre-flow" of the starting temperature

distribution, α_2 and β are the slope and exponent of the predicted temperature field, and α_3 is the "post-smoothing" of the newly released heat. The method converges as long as $0 \leqslant \alpha_1, \alpha_2, \alpha_3 \leqslant 1$ and $0 < \beta < 1$, with a few exceptions (for example, if $\alpha_1 = \alpha_3 = 0$, then H^{n+1} is discontinuous and the performance is very poor). Numerical experiments and the heuristic reasoning of Section 2 show that the most effective values are

$$\alpha_1 = 1, \qquad \alpha_2 = \alpha_3 = \tfrac{1}{2}, \qquad \beta = \tfrac{1}{2},$$

as presented above.

3.2. Finite Mobility

In the above context, it is very simple to implement a finite coefficient of kinetic mobility $\alpha(\mathbf{n}) > 0$ as in (8). Let us write the anisotropic kinetic coefficient as

$$\alpha(\mathbf{n}) = \bar{\alpha} f_\alpha(\mathbf{n}),$$

where f_α has average value 1. Then we modify (25) to

$$H^n = G_{\Delta t} * u_n + (2\pi\, \Delta t)^{-1/2}\, \rho_n + \bar{\alpha}\, \Delta t^{-1}\, \tilde{\rho}_n,$$

in which the anisotropic distance function is

$$\tilde{\rho}_n(x) = f_\alpha(\mathbf{n}(x))\, \rho_n(x),$$

$$\mathbf{n}(x) = \operatorname{sgn}(\rho_n(x)) \frac{x - x_*}{|x - x_*|},$$

where x_* is the foot of x in Γ_n; if x is near Γ_n, then $\mathbf{n}(x)$ is roughly the local outward-pointing normal to Γ_n. For x on a candidate smooth interface Γ close to Γ_n,

$$H^n(x) \approx u^n_\Sigma(x) + \frac{\alpha(\mathbf{n})}{\Delta t} \rho_n(x).$$

The stationarity condition (26) is then approximately

$$u_{n+1}(x) + \alpha(\mathbf{n}) \frac{\rho_n(x)}{\Delta t} + \bar{\sigma} \mathscr{K}_\sigma = 0$$

and the velocity-dependent Gibbs–Thomson relation (8) emerges in the limit $\Delta t \to 0$. This is essentially the approach used to define motion by weighted mean curvature for general non-smooth energy functions in [34] (using isotropic α).

Note that, for the discrete-time problem as for the original, introduction of $\alpha > 0$ is strongly regularizing; the normal slope of H^n becomes $\mathcal{O}(\Delta t^{-1})$ rather than $\mathcal{O}(\Delta t^{-1/2})$. A rigorous proof that the sequence $\{\Sigma_n\}$ converges to an evolution satisfying (8) may be found in [1].

Our belief is that mobility, especially its direction-dependence, plays a key role in producing the shapes of snowflakes, and a smaller role in determining the shapes of solids freezing from a melt. In this paper we focus on the case $\alpha = 0$; in future work we shall consider the effect of introducing mobility limitations. Note that the variation of α between different directions may be arbitrarily large; it is not necessary that $\alpha(\mathbf{n})$ be a convex function of direction.

3.3. Discrete Implementation

Finally, we briefly discuss the discrete implementation of this approximation in an actual computer program. Temperature and other functions of x are represented by their values at nodes of a uniform square grid

$$u_{ij} = u(i\, \Delta x, j\, \Delta y), \qquad i = 0, 1, \ldots, N_x, \quad j = 0, 1, \ldots, N_y.$$

When values at intermediate points are required, they are determined by bilinear interpolation. No account is taken of the interface position in representing a temperature field; since u has a discontinuous gradient, bilinear interpolation is only first-order accurate there.

The interface Γ is represented as the polygonal curve joining control points P_j, $j = 0, 1, \ldots, N-1$. The number of points changes from time step to time step as points are added or deleted. The adding and deleting are done so as to maintain spacing of consecutive points close to a specified length d_0:

$$0.7 d_0 < |P_j - P_{j+1}| < 1.5 d_0. \tag{27}$$

No account is taken of local curvature in these tolerances. An advantage of the variational formulation is that we do not have to be especially careful in this adding and deleting, since the primary information controlling the position of the interface is stored in the temperature field; for example, numerical viscosity as discussed in [30] is not a concern. We demonstrate this in our example calculations below.

One disadvantage of this representation is that changes of topology are difficult to implement; in three dimensions they would be nearly impossible. As our computations in Section 4 show, much interesting behavior happens before any topology changes are necessary. Also, note that the algorithm we have presented does not impose any particular discrete representation; a different one could be introduced if desired for particular reasons.

The discretization parameters are therefore the time step Δt, the grid spacings Δx and Δy, and the point spacing d_0. We usually take $d_0 = \Delta x = \Delta y$, so that there is only one parameter for time discretization and one for space discretization.

The first task is to compute the distance function $\rho_n(x)$ at each grid point. This is easily done by using a linear

approximation to the distance function for each segment of Γ_n in the appropriate wedge of validity. At each step, we need values only in a narrow stip around Γ_n. Since $\rho_n(x)$ is smooth, bilinear interpolation is adequate between grid points.

For the minimization, we use the techniques developed in [5]. The minimum is sought among displacements of the control points along local normal vectors. That is, if $\mathbf{n}_j$, $j=0, 1, \ldots, N$, are a suitable discrete approximation to the local normals, the candidate new interfaces are the polygons joining

$$P_j(\lambda) = P_j^0 + \lambda_j \mathbf{n}_j.$$

Approximation of the energy function $\mathscr{E}^n(\Gamma)$ gives an energy function $E(\lambda)$ on R^N, which is minimized by a modified Newton's method. Note that we never have to compute the whole integral $\int_\Omega H^n$; for Newton's method we need only the gradients and Hessian matrix which are local functions of the point positions. Since the Hessian $\mathscr{H}$ is tridiagonal, the linear algebra is straightforward; we use a solver written and generously shared by Maurizio Paolini, which performs modified Cholesky decomposition when $\mathscr{H}$ is not positive definite. For small Δt, the starting position Γ_n is very close to the minimum, and although $E(\lambda)$ is only C^1 due to the bilinear interpolation of H^n, the minimum is typically attained after four or five iterations. We do not perform any line search, and an indefinite $\mathscr{H}$ is rarely encountered.

When the minimum has been reached, a "respace" routine is called which adds and deletes points to maintain the constraints (27). This perturbs the interface position, but freedom to make this kind of perturbation is one of the primary advantages of using a variational formulation, as we demonstrate in Section 4.

In computing the heat released onto the square grid by the motion from one polygonal interface configuration to another, we use a "volume fraction" routine. Given a polygonal interface, this determines for each cell of the grid, the exact fraction of the area of that cell which is inside the interface, and partitions that area among the nodes at the four corners in proportions determined by the first moments of the area within the cell. That is, it goes from a geometrical representation of a region Σ to a grid representation of the characteristic function χ_Σ, exactly preserving the area $|\chi|$ and the three first moments $\int_\chi x$, $\int_\chi y$, and $\int_\chi xy$. The difference of characteristic functions is taken on the grid and added to the temperature field.

Solving the heat equation on a square grid is an extremely standard task, and quite straightforward in this case of equal diffusion coefficients. If the time step Δt is short, we take a suitable number of steps with the explicit method (since this takes few operations per node and vectorizes very well, it is often the method of choice for the time steps of interest). If a longer time step is required, we use the fully implicit method, solving the resulting linear equations by Fourier transform in one direction (x or y) coupled with a tridiagonal solver in the other. Higher-order time discretizations such as Crank–Nicholson, or splittings such as alternating direction implicit, do not give acceptable results for this problem, since part of the initial data at each step (the difference of characteristic functions) is far from smooth. On any reasonably-sized grid, solving the heat equation is the most time-consuming part of the calculation.

The resulting code contains a great deal of geometric complexity. This is managed by using the C++ object-oriented programming language, which permits definition of "classes" such as points, vectors, loops of points to represent the interface, etc. Once fundamental operations are defined for each class, the classes may easily and safely be combined in many different ways. Because data local to each class is well-hidden, there is not the explosion of complexity which would result if Fortran or even C were used.

4. COMPUTATIONAL EXAMPLES

We now present results obtained by the algorithms described in Section 3, in two space dimensions. We shall first present test examples which verify the correctness of the code, then compute some interesting and realistic dendrite shapes.

4.1. Circular Symmetry

The first test we perform is to reproduce the exact spherical solutions (12), (13) for $\sigma = 0$ presented in Section 1. We may easily set $\sigma = 0$ in our computation without violent instability, if we prescribe circular initial data and at each step search for a minimizing configuration only among circular configurations with specified center. This problem is thus an excellent test of the heat-release, heat-flow, and minimization parts of the algorithm, with a minimum of geometrical complexity.

We take the undercooling $u_\infty = -\frac{1}{2}$, for which (15) gives $S = 1.56$. We run the computation from $t = 1$ ($R = 1.56$) to $t = 2$ ($R = 2.21$). The domain size is 16×16 with insulating boundary conditions for temperature; for these parameters, the maximum temperature of the exact solution on the boundary at $t = 2$ differs by only 10^{-4} from u_∞, so the finite domain size does not affect the growth of the seed. With the point spacing d_0 equal to the grid spacing Δx, the only computational parameters are Δx and Δt. As a function of these parameters, the error in final radius is shown in Table I.

The algorithm is more or less converging toward the correct solution as the computation is refined, although the rate is rather irregular. These data and others indicate that the rate of convergence is generally half-order in Δx and Δt. In this test, the minimization subroutine is almost never

TABLE I

Radius Error—Frank Sphere Solutions

	Δt				
Δx	0.05	0.02	0.01	0.005	0.002
0.2	0.083	0.040	0.010	−0.018	−0.078
0.1	0.063	0.0052	0.035	0.019	−0.0089
0.05	0.067	0.037	0.024	0.0021	0.015
0.02	0.068	0.039	0.026		

satisfied with its convergence to a minimum, causing the size of the error to be very erratic. We believe this is due to poor approximation of the gradient and Hessian of the energy function; the discrete expressions used are only approximately consistent with each other due to the non-smoothness of the integrand $H^n(x)$ as represented on the finite grid (H^n is piecewise bilinear, hence only C^0). The full-scale computations below do not show this reluctant convergence, thus these poor results are not indicative of the general performance of the algorithm.

We now illustrate the robustness of the variational algorithm to perturbations of the interface position. We again run the Frank-sphere test problem, taking $\Delta x = 0.1$, $\Delta t = 0.01$, except that at $t = 1.3$ we "kick" the interface: after finding the minimum but before releasing the new heat, we increase the radius by 0.02. The radius error as a function of time is shown in Fig. 1; following the kick, the error rapidly returns to close to its value in the absence of perturbation.

This happens because the information which determines successive interface position is stored primarily in the temperature field rather than in the previous positions. When the radius is suddenly increased, heat is released, the neighborhood of the interface becomes hot, and the interface retreats on subsequent steps. In this mechanism, it is essential that heat be conserved exactly; as discussed in Section 2, it is an essential feature of this problem that we may never contemplate motion of the interface without associated heat release or absorption. It is because of this robustness that we may add and delete points at will to maintain the spacing criterion (27).

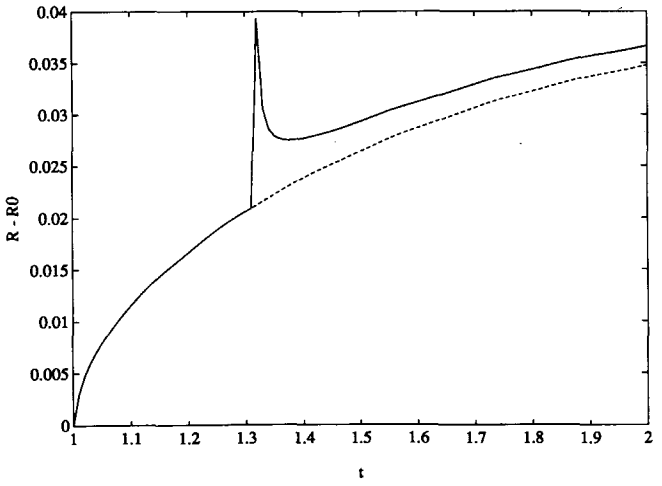

FIG. 1. Robustness of variational algorithm. The graph shows the radius error, relative to the exact solution, for a circularly symmetric interface. In the run shown by the solid line, the interface is "kicked" at $t = 1.3$. Because heat is exactly conserved, the error decreases following the perturbation, returning to nearly its unperturbed value (dashed line).

4.2. Isotropic Surface Energy

All the large-scale computations we present here are performed on a 40×40 spatial domain, with insulating (homogeneous Neumann) boundary conditions for temperature. The initial temperature is always $u_\infty = -\frac{1}{2}$ outside the seed, and zero inside. The initial configuration is always an irregular polygon of radius roughly 0.1. The computation is stopped when any temperature value on the boundary rises to $\frac{1}{2}u_\infty$, indicating that the presence of the boundary is beginning to affect the seed growth.

We always take no kinetic limitation, $\alpha = 0$; the only feature which varies between our four different examples is the magnitude and anisotropy of the surface energy σ. In future work we shall carry out the program presented in the Introduction by exploring the effect on the interface morphology of varying the undercooling and the magnitude and anisotropy of α.

We always use the time step $\Delta t = 0.01$; in all computations except the last ($\sigma = 0.001$) the grid is 400×400; thus

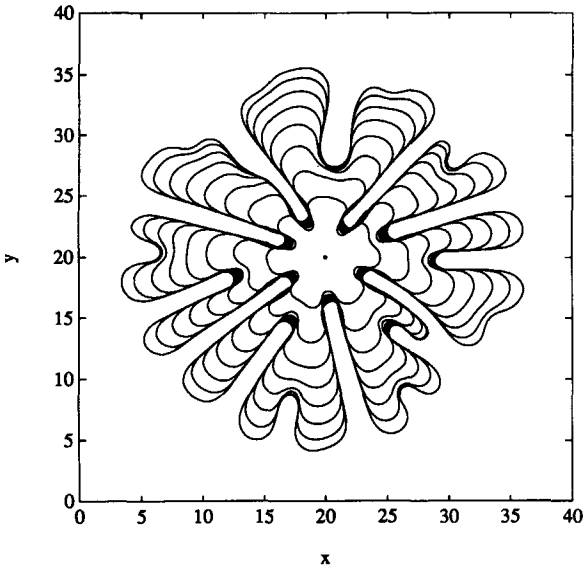

FIG. 2. Isotropic surface energy: $\sigma = 0.002$. This is the "tip-splitting" structure characteristic of radial growth with no material anisotropy, starting from the initial speck in the center. We plot the interface at time intervals of 5; the final time is 40.

the grid spacing and point spacing are $\Delta x = d_0 = 0.1$. All computations were performed on a Silicon Graphics Iris 4D-50GT workstation.

For the first example, we take isotropic surface energy, of magnitude $\sigma = 0.002$. The resulting shape is shown in Fig. 2. We see the "tip-splitting" instability characteristic of radial growth with no material anisotropy, as in Hele–Shaw flow (see [18]). The final interface configuration has 2999 points; the computational time is about 22 h.

In Fig. 3, we show a few early stages in the initial growth of the seed. The initial conditions are an irregular hexagon of radius $R = 0.1$. By $t = 0.1$ (10 computational steps) the hexagon has become nearly a circle, of radius $R = 0.58$. As the seed grows, it maintains a roughly circular shape, but the small perturbations left over from the initial data gradually grow by the Mullins–Sekerka instability mechanism (Section 1). At $t = 1$, six bumps are visible; these correspond to the six vertices of the initial shape and grow into the six major arms of Fig. 2.

The approximate formula (16) gives $R_{\text{crit}} \approx 0.12$ for $m = 6$ and $S = 1.56$ corresponding to $u_\infty = -\frac{1}{2}$. Since this seed is evidently stable to linear perturbations up to around $R = 0.6$, and unstable for larger R, we conclude that (16) is accurate only to within about a factor of 5.

The detailed structure of the initial data is quickly washed out as the seed settles into the "attracting" circular shape determined by the surface energy; the only role of the initial data is to supply the initial perturbation to the intrinsic instability mechanism. With isotropic surface energy, no mode or orientation is inherently preferred; the mode and orientation of the initial instability come from the starting shape. In this sense information from the initial conditions survives into the final structure. Contrast this with Figs. 4b and 5.

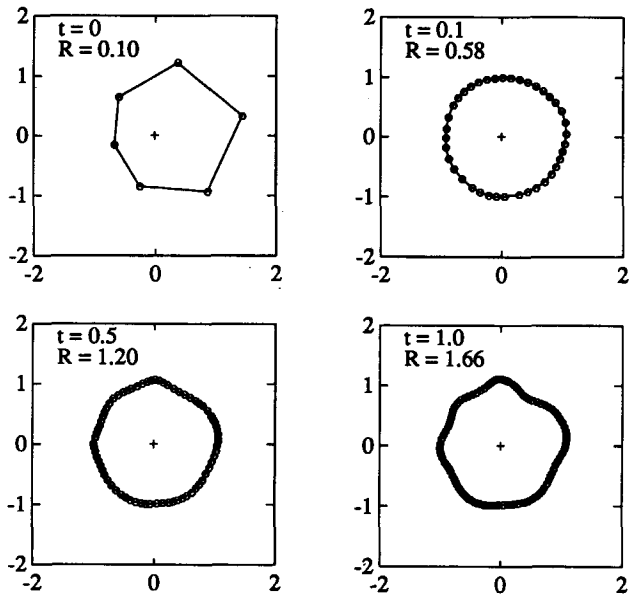

FIG. 3. Isotropic surface energy $\sigma = 0.002$: Early stages. We show several stages in the initial evolution of Fig. 2. The pictures have been scaled so that each has the same area as the unit circle; the radius R is the scaling factor, that is, the radius of a circle with the same area. The small circles represent computational node points, which are maintained with spacing near $d_0 = 0.1$.

4.3. Anisotropic Surface Energy

For anisotropy with mode number m, we take surface energy of the form

$$\sigma(\theta) = \bar{\sigma} \cdot (1 + \delta_1 \cos m(\theta - \phi) + \delta_2 \cos 2m(\theta - \phi)), \quad (28)$$

where θ is the angle of the local normal vector measured counterclockwise from the positive x-axis, $\bar{\sigma}$ is the average magnitude of the surface energy, and ϕ is a phase angle. We take the coefficients to be

$$\delta_1 = \frac{4}{3}\frac{1}{m^2 - 1}, \qquad \delta_2 = -\frac{1}{3}\frac{1}{4m^2 - 1},$$

since for these values the surface tension (22) is

$$\sigma''(\theta) + \sigma(\theta) = \tfrac{8}{3}\bar{\sigma} \sin^4 \tfrac{1}{2}m(\theta - \phi)$$

with a fourth-order zero at $\theta - \phi = 2n\pi/m$. Thus these values give the "most anisotropic" function of the form (28) for which the surface tension is nonnegative. In geometrical terms, the motivation for introducing the second term in (28) is to sharpen the corners of the Wulff shape and more closely mimic a crystalline material whose equilibrium shape is actually a polygon. The vanishing of the surface tension at isolated angles does not appear to cause any computational difficulties.

We show three examples, all with $m = 4$ and with $\bar{\sigma} = 0.005, 0.002, 0.001$. The results are shown in Figs. 4a, b, and c. In these three examples, we have chosen the phase angle $\phi = \pi/4$, so that horizontal and vertical faces are mildly preferred over diagonal ones. This choice causes the dentritic arms to extend diagonally, letting them go for longer before reaching the box corners. As a check of the effect of the underlying square grid, we have performed the same computations with $\phi = 0$ so that the arms extend horizontally and vertically; the shapes and quantitative checks below are similar. In Figs. 4a and b, the final interfaces have around 2000 points, and the computation times are about 8 h. In Fig. 4c, a finer 600×600 grid is required; the final interface has 6484 points and the computation time is about 12 h.

The resulting shapes differ dramatically from Fig. 2. Four major arms emerge in the diagonal directions determined by the interface anisotropy. From the spacing of successive time slices, it is clear that the tips of the arms are moving at

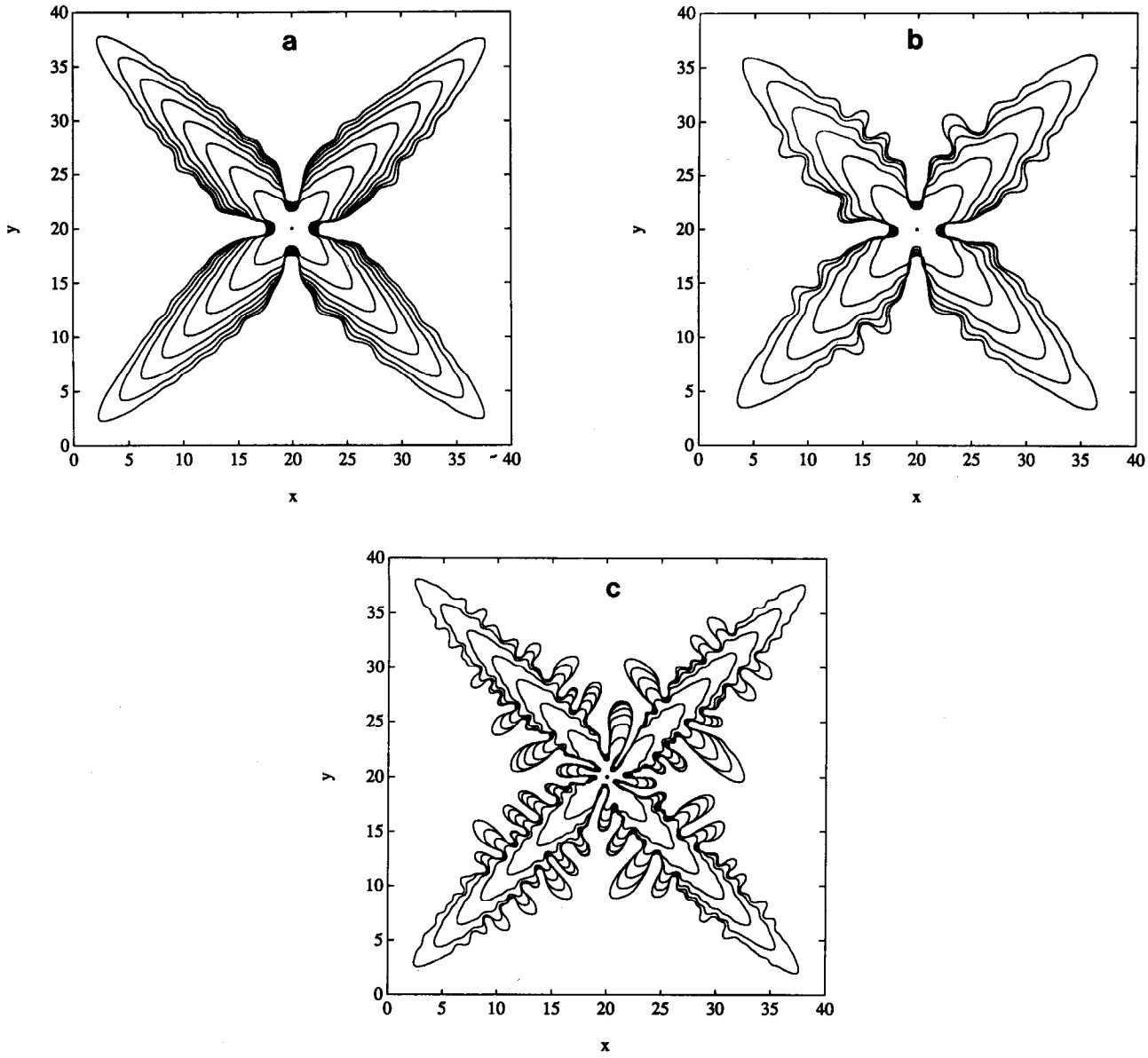

FIG. 4. a. Four-fold anisotropy: $\sigma = 0.005$. By contrast to Fig. 2, four strong arms appear, their number and directions determined by the surface energy function; these arms grow much more rapidly than the radially symmetric structure. Side-branching instability is barely visible. Time interval is 2.5; maximum time is 21.3. b. Four-fold anisotropy: $\sigma = 0.002$. With smaller surface energy, the side branching is more developed. Time interval is 4; maximum time is 27.1. c. Four-fold anisotropy: $\sigma = 0.001$. The side-branching is well developed, and we see competition among neighboring side fingers. Note the four small "vestigial" arms; these are generated by the irregularity of the initial seed but lose to the large arms because their directions are unfavored by surface energy. Time interval is 2; maximum time is 14.9. Growth is twice as rapid as in Fig. 4b.

roughly constant velocities and that they have reached steady-state parabolic shapes. As the surface energy is reduced, more structure appears. The final shape in Fig. 4c is very similar to dendritic profiles observed in experiments [11].

In Fig. 5, we show the early stages of development for the case $\bar{\sigma} = 0.002$ in Fig. 4b. Here, the initial shape is an irregular pentagon; under the influence of surface tension, the seed rapidly assumes a roughly square shape, then becomes unstable to a perturbation whose mode number $m = 4$ and orientation are determined by the surface energy function. In contrast to Figs. 2 and 3, the large-scale structure which ultimately develops has absolutely no memory of the initial conditions. This appears to be a consequence of the anisotropic surface energy, which provides an intrinsic preference to outweigh the weak influence of the initial conditions.

The first quantitative test we can apply is to measure the

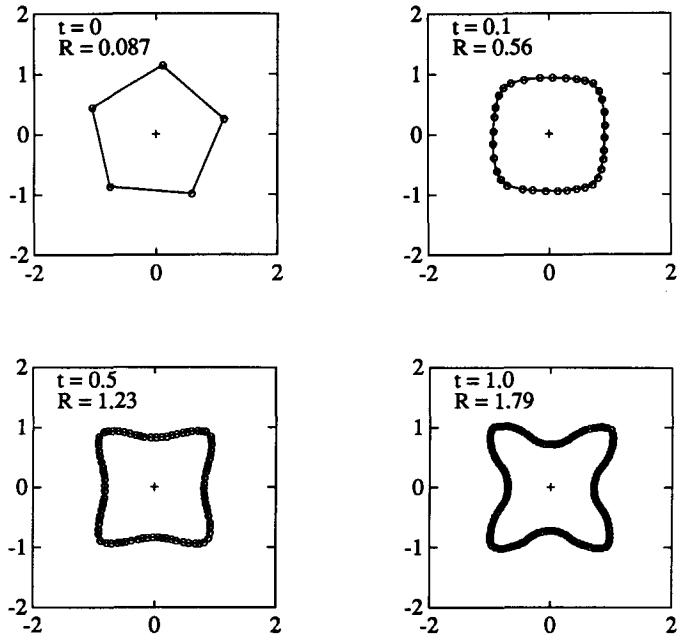

FIG. 5. Four-fold surface energy, $\sigma = 0.002$: Early stages. By contrast to Fig. 3, no memory is retained of the initial pentagonal shape; it is swamped by the four-fold anisotropy of the surface energy.

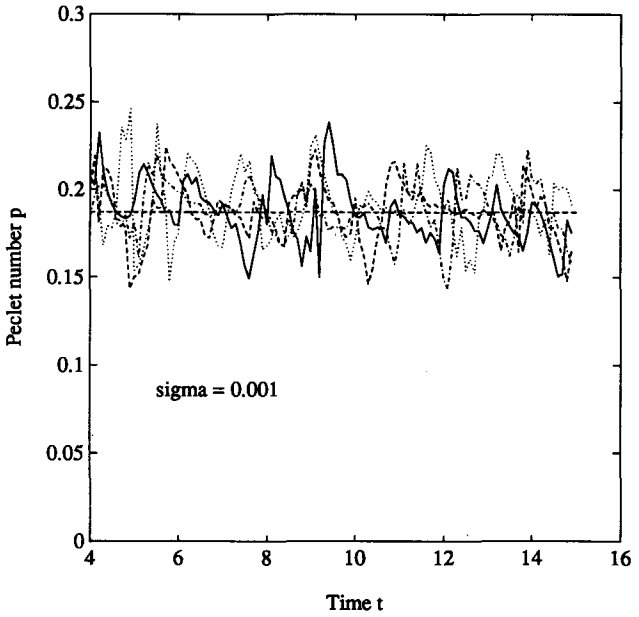

FIG. 6. Comparison to Ivantsov solution: $\sigma = 0.001$. We plot the approximate Peclet number $p = \frac{1}{2}\rho V$ for the computation of Fig. 4c, for $t > 4$ when the parabolic tip structure has established itself. The four different lines are the four tips. The dashed horizontal line shows the Ivantsov value $p = 0.187$. Despite the noise in the signal, the fit is evidently quite good.

tip velocities and curvatures, and compare the Peclet numbers (17) with the value corresponding to the Ivantsov solutions of Section 1: relation (18) gives $p = 0.187$ for $u_\infty = -\frac{1}{2}$. These quantities are easily determined by least-squares fitting of a parabola to the tip profile. In Fig. 6, we plot the numerically determined value of p for the third example, $\bar{\sigma} = 0.001$. The numerical noise is to be expected, since we are doing a polynomial fit to each time step independently and then differencing in time. The agreement is evidently quite good. In Table II, we display time-averaged values of tip curvature ρ, tip velocity V, and Peclet number p for the three cases. In each, we take a time average (following an initial transient period) and average over the four tips of each run. The values of the Peclet numbers are remarkably good; in the worst case the error is 6%.

The second quantitative test we may apply is to observe that in the original partially nondimensionalized system (3) and (4), σ is the only parameter appearing; it has the dimensions of length. Thus, for a given undercooling and a given direction dependence of $\sigma(\mathbf{n})$, all lengths in the problem must be proportional to $\bar{\sigma}$. Time must scale like $\bar{\sigma}^2$ to preserve the diffusivity $D = 1$; hence velocities should scale as $\bar{\sigma}^{-1}$. Looking at Table II, we see that we have the proper scaling in going from $\bar{\sigma} = 0.002$ to $\bar{\sigma} = 0.001$: the tip radius ρ is halved, and the velocity V is doubled. However, the case $\bar{\sigma} = 0.005$ is not consistent with this scaling.

We may also look at the spacing of side branches on the dendritic tips. This spacing presumably has some complicated dependence on undercooling, but must be simply proportional to surface energy. An extremely rough eyeball counting of local maxima shows eight small bumps on the side of the arms in Fig. 4a, six in Fig. 4b, and 12 in Fig. 4c, with corresponding spacings 2.5, 3.33, and 1.67. Again, the second and third computations are in agreement with each other and with the dimensional structure of the problem; the first simply appears to be wrong despite its correct appearance. Note that, whereas analysis of the Peclet number is a comparison with a zero-surface-energy solution, and so might be expected to be inaccurate for the larger value of $\bar{\sigma}$, the dimensional analysis has no such restriction. Note also that the three cases of Figs. 4a, b, and c are in fact the same problem on different length and time scales; treating them as different provides a valuable check on the accuracy of the numerics.

TABLE II

Dendrite Tip Properties

$\bar{\sigma}$	ρ	V	p
0.005	0.344	1.136	0.195
0.002	0.467	0.851	0.198
0.001	0.240	1.590	0.189

Presumably the first computation is underresolved in some sense, despite its agreement with the Ivantsov model. Evidently the Peclet product is a more fundamental quantity than either the radius or the velocity, since it depends on the structure of the diffusion field over a large neighborhood of the tip; it is entirely plausible that numerical error could produce wrong values of ρ and V while respecting p. These computations and a few others may be seen on video in [4].

CONCLUSIONS

We have presented a completely new variational algorithm for numerically solving the model equations describing dendritic solidification. This method has no constraints on the value of the velocity-kinetic coefficient, and hence it is able to model a natural physical regime which so far has been completely inaccessible to numerical computation.

We have computed dendritic structures with isotropic and anisotropic surface energy functions, with initial conditions of a very small irregular seed, intended to mimic snowflake nucleation in the atmosphere. With isotropic surface energy, the asymmetries of the initial conditions provide initial perturbations for the Mullins–Sekerka instability, and thus propagate into the large-scale structure. With anisotropic surface energy, the material properties force the growing solid into a characteristic shape in which the initial conditions are completely forgotten.

For anisotropic energy, parabolic dendrite tips emerge. We have quantitatively checked tip radii and velocities and compared them against exact Ivantsov solutions, obtaining agreement within a few percent.

In future work, we intend to investigate the effects of anisotropic mobility, ultimately to obtain a complete catalog of crystal shapes as functions of a few environmental and material parameters.

ACKNOWLEDGMENTS

This project described in this paper was begun and carried out under the auspices of the Minimal Surface Team of the National Science and Technology Research Center for the Computation and Visualization of Geometric Structures in Minneapolis, supported by the National Science Foundation via NSF DMS-8920161-02 and the University of Minnesota. The related work of other members and collaborators Fred Almgren and Jean Taylor has been cited above. In addition, I thank John Sullivan and Andy Roosen for helpful conversations, and the director and staff of the Geometry Center for their hospitality. The motivation to develop the method of Section 3 came from exposure to the work of Maurizio Paolini and Claudio Verdi of the University of Pavia on the prescribed mean curvature problem; I thank them for a pleasant visit there and many useful conversations. Much of the work was performed at the Courant Institute of Mathematical Sciences with support from the Applied Mathematical Sciences Program of the U.S. Department of Energy under Contract Number DE FG02-88ER25053, and from an NSF Mathematical Sciences Postdoctoral Research Fellowship.

REFERENCES

1. F. Almgren, J. Taylor, and L. Wang, *SIAM J. Control Optim.* **31** (1993).
2. F. Almgren and L. Wang, Mathematical existence of crystal growth with Gibbs–Thomson curvature effects, in preparation.
3. R. Almgren, *Computing Optimal Geometries*, edited by J. E. Taylor, Selected Lectures in Mathematics, report and video (Amer. Math. Soc., Providence, RI, 1991), p. 6.
4. R. Almgren, in J. E. Taylor, editor, *Computational Crystal Growers Workshop*, edited by J. E. Taylor, Selected Lectures in Mathematics, report and video, (Amer. Math. Soc., Providence, RI, 1992), p. 13.
5. G. Bellettini, M. Paolini, and C. Verdi, Convergence of discrete approximations to sets of prescribed mean curvature, preprint.
6. G. Belletini, M. Paolini, and C. Verdi, Front-tracking and variational methods to approximate interfaces with prescribed mean curvature, preprint.
8. D. Bensimon, P. Pelcé, and B. I. Shraiman, *J. Phys.* **48**, 2081 (1987).
9. G. Caginalp, *Phys. Rev. A* **39**, 5887 (1989).
10. R. D. Doherty, in *Crystal Growth*, edited by B. R. Pamplin, 2nd. ed. (Pergamon, Oxford, 1980), p. 485.
11. A. Dougherty, P. D. Kaplan, and J. P. Gollub, *Phys. Rev. Lett.* **58**, 1652 (1987).
12. F. C. Frank, *Proc. R. Soc. A* **201**, 586 (1950).
13. J. W. Gibbs, in *Collected Works*, Vol. 1 (Longmans, Green, New York, 1928), p. 229.
14. E. Guisti, *Minimal Surfaces and Functions of Bounded Variation* (Birkhäuser, Basel, 1984).
15. P. V. Hobbs, *Ice Physics* (Oxford Univ. Press, London, 1974).
16. G. P. Ivantsov, *Dokl. Akad. Nauk SSSR* **58**, 567 (1947).
17. D. A. Kessler, J. Koplik, and H. Levine, *Phys. Rev. A* **33**, 3352 (1986).
18. D. A. Kessler, J. Koplik, and H. Levine, *Adv. Phys.* **37**, 255 (1988).
19. R. Kobayashi, in *Computational Crystal Growers Workshop*, edited by J. E. Taylor, Selected Lecture in Mathematics, report and video (Amer. Math. Soc., Providence, RI, 1992), p. 67.
20. T. Kobayashi, *Philos. Mag.* **6**, 1363 (1961).
21. J. S. Langer, *Rev. Mod. Phys.* **52**, 1 (1980).
22. S. Luckhaus, *Euro. J. Appl. Math.* **1**, 101 (1990).
23. F. Morgan, *Riemannian Geometry: A Beginner's Guide* (Jones & Bartlett, Boston, 1992).
24. W. W. Mullins and R. F. Sekerka, *J. Appl. Phys.* **34**, 323 (1963).
25. W. W. Mullins and R. F. Sekerka, *J. Appl. Phys.* **35**, 444 (1964).
26. U. Nakaya, *Snow Crystals: Natural and Artificial* (Harvard Univ. Press, Cambridge, MA, 1954).
27. A. Roosen, in *Computational Crystal Growers Workshop*, edited by J. E. Taylor, Selected Lectures in Mathematics, report and video (Amer. Math. Soc., Providence, RI, 1992), p. 89.
28. A. Roosen, *Modeling Crystal Growth in a Diffusion Field with Fully-Facetted Crystals*, Ph.D. thesis, Mathematics Department, Rutgers University, 1992.
29. P. G. Saffman and G. I. Taylor, *Proc. R. Soc. London Ser. A* **245**, 312 (1958).

30. J. A. Sethian, *Commun. Math. Phys.* **101**, 487 (1985).
31. J. A. Sethian and J. Strain, *J. Comput. Phys.* **98**, 231 (1992).
32. J. S. Shah, in *Crystal Growth*, edited by B. R. Pamplin, 2nd ed., (Pergamon Press, Oxford, 1980), p. 301.
33. J. Strain, *SIAM J. Appl. Math.* **50**, 1 (1990).
34. J. E. Taylor, *Acta Metall. Mater.* **40**, 1475 (1992).
35. J. E. Taylor, J. W. Cahn, and C. A. Handwerker, *Acta Metall. Mater.* **40**, 1443 (1992).
36. W. Thomson, *Proc. R. Soc. Edinburgh* **7**, 63 (1870).
37. A. Visintin, in *Proceedings of a Symposium on Material Instabilities in Continuum Mechanics*, edited by J. Ball (Clarendon, London/ New York, 1988).
38. A. A. Wheeler, B. T. Murray, and R. J. Schaefer, "Computation of Dendrites Using a Phase Field Model, Technical Report NISTIR 4894, National Institute of Standards and Technology, 1992.
39. E. Yokoyama and T. Kuroda, *Phys. Rev. A* **41**, 2038 (1990).